UNIVERSITY OF CALIFORNIA,
IRVINE

Methodology to Model Aircraft and Propulsor Performance of Advanced Air Mobility

THESIS

submitted in partial satisfaction of the requirements
for the degree of

MASTER OF SCIENCE

in Mechanical and Aerospace Engineering

by

Jessica J. De la Cruz

Thesis Committee:
Professor Jacqueline Huynh, Chair
Professor Haithem A. Taha
Professor Robert Liebeck

2023

DEDICATION

To God who gives me the grace to finish the work that he leads me to pursue. To my future husband and children who God will bless me with. To my parents and younger brother.

TABLE OF CONTENTS

LIST OF FIGURES

LIST OF TABLES

ACKNOWLEDGMENTS

ABSTRACT OF THE THESIS

Methodology to Model Aircraft and Propulsor Performance of Advanced Air Mobility

By

Jessica J. De la Cruz

MASTER OF SCIENCE in Mechanical and Aerospace Engineering

University of California, Irvine, 2023

Professor Jacqueline Huynh, Chair

Advanced Air Mobility (AAM) distributed propulsion vehicles are currently being proposed in industry and may be capable of flying various operations such as Short-Takeoff and Landing (STOL), Tilt-Rotor Vertical Takeoff and Landing (Tilt-Rotor VTOL) and Lift plus Cruise Vertical Takeoff and Landing (LPC VTOL). The effects of each propulsor configuration must be assessed for efficient and quiet low-altitude flight procedures. This thesis paper outlines a methodology to assess the aircraft performance of AAM vehicles with open rotor configurations by predicting operating states such as propeller RPM, power, thrust and drag characteristics within a given flight procedure. Such methodology utilizes a polar drag buildup to predict the aerodynamic losses of AAM vehicles during takeoff, transition and cruise conditions. MATLAB is utilized to generate a best-fit line of wind tunnel-tested experimental data from parallel, normal and inclined flow to compute the coefficient of drag. Simultaneously, this methodology utilizes the blade element momentum theory propeller design program XROTOR to size the distributed propulsors capable of operating the mentioned relevant flight segments. The propulsor design methodology outlined in this paper minimizes induced losses at the rotors by constraining a low Mach tip number, to lower community noise levels with a feasible motor torque. Propeller off-design conditions are presented in propeller contour maps obtained from XROTOR for fixed and variable pitch propeller settings, to provide the mentioned relationship between RPM and segment thrust. Such a relationship

can be used to build flight procedure dynamics and predict overall efficiency and community noise levels. An application of the described methodology will be presented to determine the low-altitude flight aircraft performance of STOL, Tilt-Rotor VTOL, and LPC VTOL AAM vehicles.

NOMENCLATURE

a	=	Acceleration
a_s	=	Speed of Sound
A	=	Propeller Area
AAM	=	Advanced Air Mobility
AR	=	Aspect Ratio
C_D	=	Total Drag Coefficient
C_{Di}	=	Induced Drag Coefficient
C_{Do}	=	Zero-lift Drag Coefficient
$C_{Do-\theta}$	=	Zero-lift drag of plate at an angle
C_{Dt}	=	Distributed Propulsion Blown Drag Coefficient
C_f	=	Skin Friction Coefficient
C_J	=	Jet Momentum Coefficient
C_L	=	Lift coefficient
C_{LMAX}	=	Maximum lift coefficient
d_f	=	Fuselage Diameter
D_i	=	Induced Drag Force
D_p	=	Parasitic Drag Force
e	=	Oswald Efficiency Factor
f_b	=	Fraction of the Wing Blowing
FF	=	Form Factor

FR	$=$	Fitness Ratio
ft	$=$	Feet
$\frac{h}{b}$	$=$	Height to Span Ratio
$\frac{h_d}{c}$	$=$	Height of the Disk Normalized by the Wing Chord
$\frac{h_j}{c}$	$=$	Height of the Jet stream Normalized by the Wing Chord
l_f	$=$	Fuselage Lenght
LPC	$=$	Lift Plus Cruise
M_{tip}	$=$	Rotor Tip Mach Number
n_{prop}	$=$	Number of Propellers
R_{prop}	$=$	Rotor Radius
r_{hub}	$=$	Rotor Hub Radius
RPM	$=$	Revolutions per Minute
$STOL$	$=$	Short Takeoff and Landing
T	$=$	Thrust
$\frac{t}{c}$	$=$	Thickness to Chord Ratio
T_{engine}	$=$	Thrust Per Engine
V	$=$	Velocity
V_D	$=$	Velocity of Flow Through the Disk
V_j	$=$	Rotor Jet Velocity
V_∞	$=$	Freestream Velocity
$VTOL$	$=$	Vertical Takeoff and Landing
w	$=$	Angular Velocity
α_i	$=$	Downstream Flow Induced angle
α_0	$=$	Zero lift angle of attack
β_{pitch}	$=$	Rotor Pitch Angle
δ_f	$=$	Flap Deflection
γ	$=$	Flight Path Angle

θ $\quad=\quad$ Rotor Tilt Angle

λ_i $\quad=\quad$ Incoming Velocity Angle

ρ $\quad=\quad$ Density

$()_i$ $\quad=\quad$ Per Segment

$()_x$ $\quad=\quad$ x-Direction

$()_y$ $\quad=\quad$ y-Direction

$()^*$ $\quad=\quad$ Per Rotor

Chapter 1

Introduction

As Advanced Air Mobility (AAM) daily passenger demand is within the horizon, design development and urban infrastructure constraints have become an emerging challenge for a potential annual market valuation of 2.5 billion USD [1]. Public and private sector projects for AAM vehicles are currently being developed in the aviation industry and consequently, new emerging AAM vehicles may be capable of flying at low altitudes. Such missions include taking cargo and passengers in highly populated areas with short takeoff and landing ground distances [2]. The effects of flying each AAM configuration must be examined to understand and develop flight regulations and technology to perform this missions. Low altitude flight feasibility must be evaluated by performing other assessments, such as trajectory generation and community noise analysis. The lack of aircraft performance modeling data acquisition capabilities however has become a challenge for many developers since data is not as widely available as conventional tube and wing data. The following work aims to solve such a problem by means of presenting a framework to model AAM vehicle performance. This thesis paper describes a methodology to assess the aircraft performance of any AAM vehicle with open rotor configurations by predicting operating states such as lift, drag, thrust and RPM for any given flight procedure segment. Each AAM vehicle may feature unique geometry

with different numbers of rotors with various placement conventions, leading to unique flight capabilities, operations, emissions, and noise sources.

Various vehicle types are currently under consideration in their feasibility to perform AAM operations, including but not limited to blown-flap short takeoff and landing (Blown-Flap STOL) vehicles, tilt-rotor vertical takeoff and landing (Tilt-Rotor VTOL) vehicles, and lift plus cruise vertical takeoff and landing (LPC-VTOL) vehicles, as diagrammed in Fig. 1.1.

(a) Blown-Flap STOL   (b) LPC-VTOL   (c) Tilt-Rotor VTOL
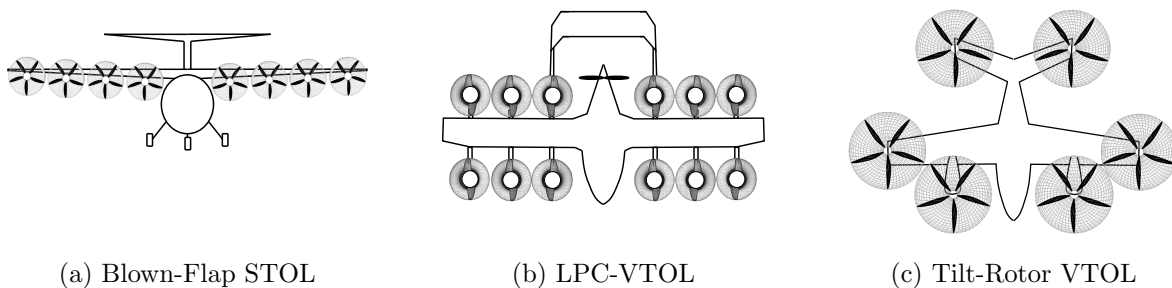
Figure 1.1: Example AAM vehicle types

The aforementioned AAM aircraft performance and propulsor modeling methodology is described and applied in the following work. The flight procedure analyzed in this paper is assumed to have a standard vertical takeoff, a transition, and level cruise segment as seen in 1.2(a). The methodology outlined in this paper outputs detailed rotor pitch blade geometry for vehicle integration to provide instantaneous rotor geometry inputs to any source noise modeling method. The rotor tilt angle θ_i and the incoming velocity λ_i seen in Fig. 1.2(b), are defined to compute the resulting vehicle lift, drag, thrust and RPM required to fly such a procedure.

(a) Flight path aerodynamic forces acting on AAM body

(b) Incoming velocity vector angles λ_i and rotor tilt angles θ_i for variable pitch propulsion
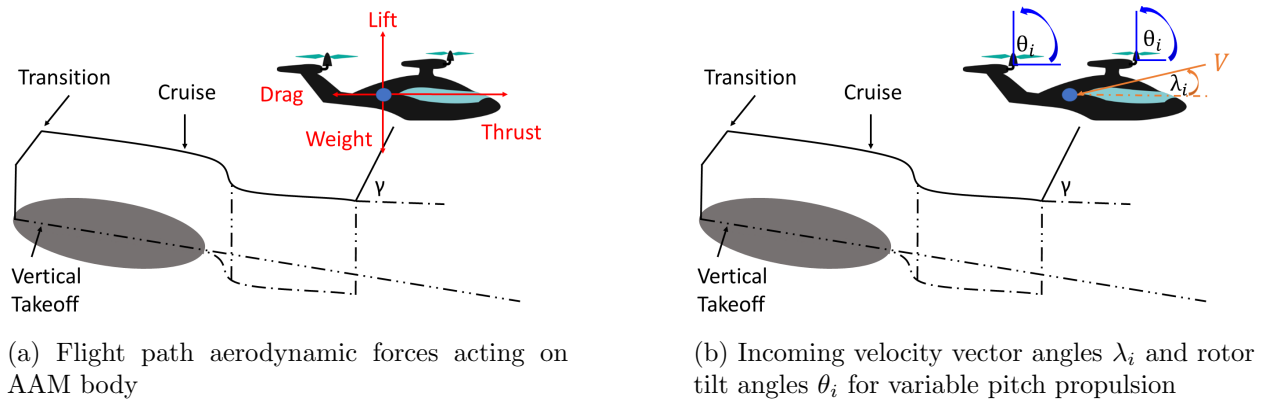
Figure 1.2: AAM Flight Procedure

Chapter 2 presents the aircraft performance framework divided into three submodels including lift and drag, as well as, the rotor performance and rotor geometry models. For each model, the background and methodology are explained in detail for obtaining the aforementioned performance characteristics. Next, Chapter 3 covers an application of such methodology for a 9 passenger Blown-Flap STOL vehicle, a 2 passenger LPC-VTOL vehicle, and a 4 passenger Tilt-Rotor VTOL. A standard AAM flight trajectory was assumed for the LPC VTOL and the Tilt-Rotor VTOL flight procedures as seen in 1.2(a). The sample demonstrations present vehicle predictions of the total drag coefficients, as well as the induced and parasitic drag forces for the vertical takeoff, transition and cruise segments. The parasitic and induced drag forces are presented for the mentioned segments for each vehicle. In addition, fixed and variable pitch propellers designed uniquely for each vehicle are shown to demonstrate propulsion prediction capabilities by utilizing the propeller design methodology outlined in this paper. Lastly, propeller contour maps are determined to show the detailed rotor performance at various velocity and RPM settings, as well as, the unfeasible thrust regions.

Chapter 2

Methodology to model aircraft performance of AAM vehicles

The methodology to model the aircraft and propulsor performance of any AAM vehicle configuration is shown in Fig. 2.1. The purpose of the aircraft performance model presented in this paper is to obtain the aerodynamic forces, as well as, the rotor performance and rotor geometry characteristics required for AAM flight. Once the segment aerodynamic forces and propeller performance is obtained, the flight procedure and source noise levels resulting from community overflight can be analyzed. An example of such modeling methodology is presented by [3] to model flight procedural source noise levels by utilizing incorporated methods from the NASA Aircraft Noise Prediction Program (ANOPP2)[4]. Such methodology propagates hemispherical source noise levels to the ground at desired observer locations, such as a population grid surrounding an airport. The methodology outlined in this paper outputs the segment aerodynamic forces, velocity, thrust, and detailed rotor blade geometry and performance, required as an input to the aforementioned flight profile modeling method and the source noise modeling method.

Given the aircraft characteristics, aircraft type and rotor geometry or design condition, along with the desired segment thrust and velocity from a preliminary assumption, the aircraft performance model outputs the magnitude of the vehicle aerodynamic forces, as well as, the RPM necessary to build the flight physics per segment for any flight procedure.
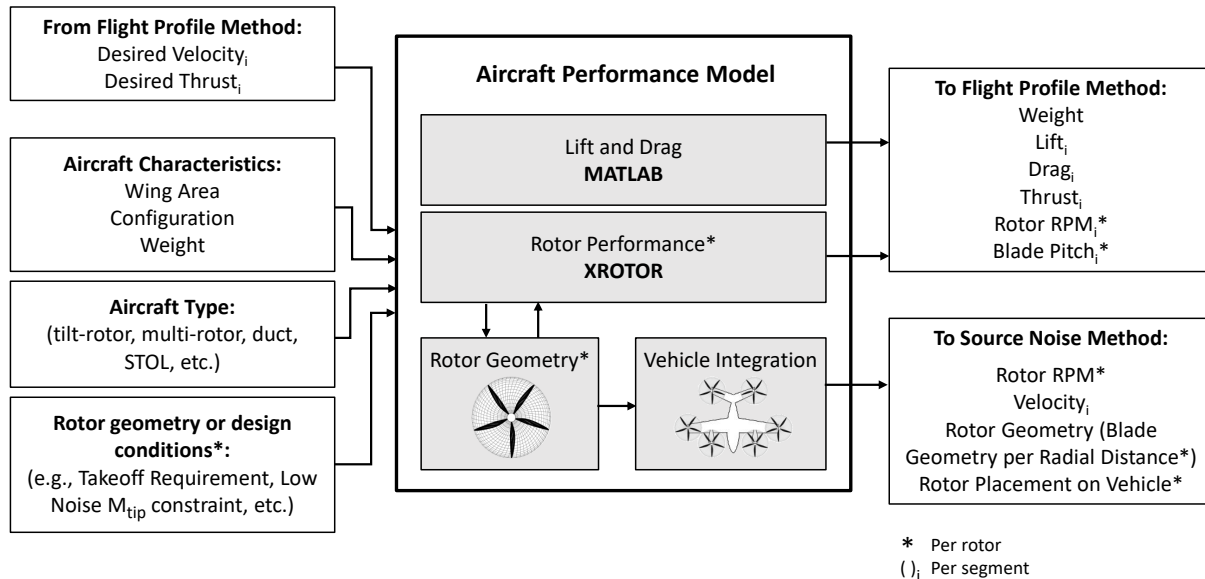
Figure 2.1: Aircraft Performance Module modeling framework

Any AAM flight procedure can be modeled by following the method from [3] to determine the aircraft state at any point. Such a method utilizes the governing physics of an arbitrary AAM vehicle and is summarized by a point mass model with component-level equations provided in eq. 2.1 and 2.2. Provided an operation definition, such as a vertical takeoff to a given altitude or a high-power climb, along with an AAM vehicle type, the mentioned flight profile segment aerodynamic loads are dependent on the geometry and the propulsive system arrangements of any vehicle architecture.

$$T_x - Drag_x - Lift_x = ma_x \qquad (2.1)$$

$$T_y - Drag_y + Lift_y - Weight = ma_y \qquad (2.2)$$

Within the Aircraft Performance Module, the thrust, lift and drag are obtained for the takeoff, climb and cruise flight segments as described in detail in the following Chapters, while the vehicle weight is assumed to be constant throughout the flight procedure. The aforementioned forces and a representative rotor geometry and RPM are obtained and sent to the flight profile modeling method. The thrust obtained from the designed fixed or variable pitch geometry propeller is presented with contour maps necessary to map the thrust magnitude per propeller at a set velocity and RPM. The rotor geometry for vehicle integration is outputted to the source noise modeling method, which requires rotor blade geometry and detailed rotor vehicle placement.

2.1   Lift and Drag

2.1.1   Lift

The lift force that originates from airfoil pressure distributions and the aerodynamic interaction of the geometry of the wing, the airflow velocity and the angle of attack, is determined with the equations provided in eq. 2.1 and 2.2, given the previously mentioned aircraft characteristics such as wing area, configuration and weight, as well as, the AAM aircraft type. Such force is determined with assumed values of the lift coefficient (C_L) during takeoff, climb and cruise segments. The lift coefficient for the cruise segment is assumed from [2]. A NACA 0010 airfoil is assumed for the transition segment with an angle of attack of 4° above the zero lift angle of attack (α_0). Likewise, an assumption is made for the ground roll coefficient

if applicable.

2.1.2 Drag

The drag force that resists the aircraft motion originates due to air and vehicle surface pressure and shear interactions. A parabolic drag buildup is utilized to predict the total coefficient of drag, consisting of the zero-lift or parasitic drag coefficient, the induced drag coefficient, and the drag coefficient due to blowing for the STOL vehicle, found in the equation shown in eq. 2.4.

$$C_D = C_{Do} + \frac{C_L^2}{\pi A R e} + C_{Dt} \tag{2.3}$$

The zero-lift drag (C_{Do}) consists of skin friction drag and pressure drag that originate due to fluid viscous effects boundary layer formation along the surface planform of the wing [5]. As the 3D wing moves through the flow however the trailing vortices cause a downwash behind the wing causing the lift vector to tilt and develop drag due to lift, namely induced drag (C_{Di}). The total drag coefficient found in eq. 2.4 does not include compressibility effects since the low altitude cruise mach number is below 0.3. The drag due to blowing (C_{Dt}) arises for vehicles with distributed propulsion blown flap high lift configurations such as the STOL vehicle analyzed in this paper. An example of this vehicle configuration is the Helio Courier, which is able to achieve STOL due to the remarkable aerodynamic capabilities of high lift devices, as defined and demonstrated in [6][7]. At low speeds, leading edge slats are deployed due to suction pressure increasing as the velocity during takeoff gradually changes. Within the slat, a vacuum cell originates by the maximum depression of the top vane of the airfoil [6]. This device provides the STOL maximum lift coefficient (C_{Lmax}) needed to

takeoff in short distances when combined with the deployment of trailing edge slotted flaps. Such devices are then retracted at higher speeds to lower drag after the takeoff segment since the great rise of C_{Dt} is unfavorable after departure. The momentum theory model of jet contraction experimentally validated in [8], computes the C_{Dt} with equations presented in eq. 2.4 to 2.10, where $\frac{h_d}{c}$ is the height of the disk or propeller diameter normalized by the wing chord, R_{prop} is the rotor radius, r_{hub} is the hub radius, A_{prop} is the propeller area, V_j is the velocity of the flow at the disk, V_D is the velocity of the flow going through the disk, $\frac{h_j}{c}$ is the height of the jetstream normalized by the wing chord, f_b is the spanwise fraction of the wing in blowing, α_i is the downstream flow induced angle, and C_J is the jet momentum coefficient.

$$\frac{h_d}{c} = \frac{\pi * (R_{prop}^2 + r_{hub}^2) * n_{prop}}{b * c} \tag{2.4}$$

$$V_j = \sqrt{\frac{2 * \frac{T}{engine}}{\rho * A_{prop}} + V_\infty^2} \tag{2.5}$$

$$V_D = \frac{V_j + V_\infty}{2} \tag{2.6}$$

$$\frac{h_j}{c} = \frac{h_d}{c} * \frac{V_D}{V_j} \tag{2.7}$$

$$CJ = 2 * \frac{V_j^2}{V_\infty} * \frac{h_j}{c} \tag{2.8}$$

$$\alpha_i = \frac{C_L}{\pi * AR * e} \tag{2.9}$$

$$CD_t = 2 * CJ * f_b * \alpha_i \tag{2.10}$$

The aforementioned parabolic drag buildup is obtained by utilizing MATLAB to model the vehicle geometry and compute the zero-lift, induced drag and the drag due to blowing if applicable, for the vertical takeoff, as well as, for the cruise and climb segments introduced in Chapter 1. Due to the nature of AAM flight procedures, such drag is computed for three different incoming flow angles of 0°, 45° and 90° to model the directional flow interactions as seen in Fig. 2.2 (a). In addition, three different propeller tilt angles seen in Fig. 2.2 (b) are also modeled to capture the effects of variable pitch propellers and the surface interactions during climb and cruise.
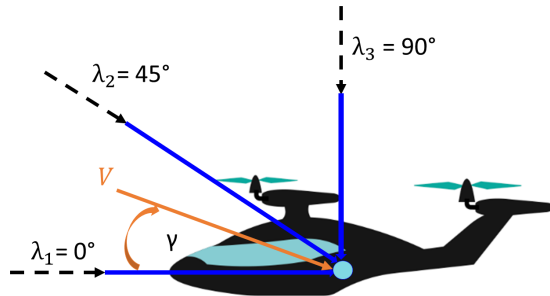
(a) Incomming velocity vector angles for cruise, climb and VTOL flight for AAM procedures
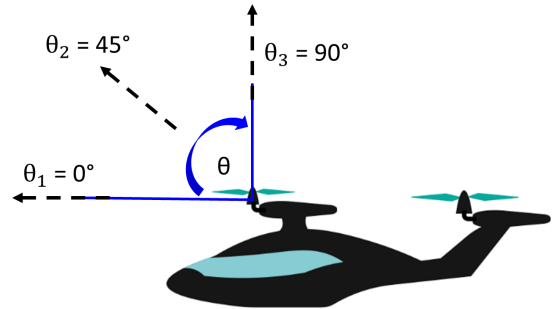
(b) Rotor tilt angles for variable pitch propulsion

Figure 2.2: AAM Velocity and rotor tilt angles for coefficient of drag analysis

For VTOL, the wing and horizontal tail are assumed to act as flat plates normal to the flow while the fuselage is assumed to act as an ellipsoid in the same manner. The zero-lift drag is obtained from a best-fit line of parasitic drag coefficient experimental data of rectangular plates in perpendilar flow, as well as, ellipsoids in normal supercritical flow as published by [9]. The area of reference for the coefficient of drag is the rectangle and ellipsoidal area normal to the incoming flow direction. The zero-lift drag experimental data is obtained as a function of the normal Reynolds number for the ellipsoid. The supercritical form of the simple ellipsoidal bodies interpolation principle is used with the equation shown in eq. 2.11, with an approximate interpolation of the skin friction coefficient $C_f = 0.004$, as suggested by [9]. Where l_f is the fuselage length and d_f is the fuselage diameter.

$$C_{Do} = 3 * C_f * (\frac{l_f}{d_f}) + 4.5 * C_f * (\frac{d_f}{l_f})^{\frac{1}{2}} + 21 * C_f * (\frac{d_f}{l_f})^2 \qquad (2.11)$$

The zero-lift drag for the rectangular plates is obtained as a function of the height-to-span ratio since the drag is independent of the Reynolds number in perpendicular flow due to the rise of separation at the edge of the plate, regardless of the boundary layer formation [10]. Since most of the change in the experimental data occurs at low height-to-span-ratio for the rectangular plate, an interpolation at such values is suggested by [9]. This interpolation is utilized for the drag of rectangular plates in normal flow by assuming a vortex sheet ventilation with the equation shown in eq. 2.12. Where CD_{o-0} is the basic zero drag coefficient at the low height-to-span ratio, k is a constant of the order of 5 and h/b is the mentioned height (or diameter) to span ratio of the rectangular plate or cylinder.

$$C_{Do} = C_{Do-0} * (1 - k * (h/b)) \qquad (2.12)$$

Due to the variable angles γ of the incoming velocity vector during each flight phase, the powered and unpowered propeller orientation with respect to the incoming velocity must be examined for drag considerations. The propeller drag force opposite to the direction of flight is neglected for powered propellers for the VTOL, transition and cruise segments, since the drag force of the powered propeller counters the torque applied to the motor shaft from skin friction on the propeller surface blades. Therefore, such drag is ingrained in the net thrust generated upward by a powered propeller if opposite to the direction of motion. However, if un-powered the methodology in this paper suggests to model either as a circular plate in normal flow or a stopped propeller in normal flow with a best-fit line from experimental data also found in [9]. For a vectored thrust fixed pitch propeller that is un-powered and parallel to the flow, the zero-lift coefficient of rotor drag must be modeled as a flat plate, as per the convention.

For the cruise horizontal flight, the drag buildup utilizes conventional form factor FF equations for wing and streamlined bodies given by eq. 2.13 and 2.14, found in [9], where FR is the fineness ratio of the streamlined body and t/c is the thickness to chord ratio of the lifting surface.

$$FF = 1 + \frac{1.5}{FR^{1.5}} + \frac{7}{FR^3} \tag{2.13}$$

$$FF = 1 + 2 * (\frac{t}{c}) + 60 * (\frac{t}{c})^4 \tag{2.14}$$

For climbing flight, the plate at an angle principle also by [9] is utilized to obtain the zero-

light drag as a function of the climb flight path angle. This principle is provided by the equation shown in eq. 2.15. Where $C_{Do-\theta}$ is zero-lift drag of the plate at an angle and γ_i is the incoming velocity angle from the horizontal direction to the plate or lifting surface angle.

$$C_{Do-\theta} = C_{Do} * sin\gamma_i \qquad (2.15)$$

The induced drag is determined from the given aircraft geometry, desired velocity, and segment lift coefficient while if applicable, the drag due to blowing is added to such buildup.

2.2   Thrust

The thrust force that drives the aircraft originates from the reaction obtained by the propeller blades cutting through a fluid medium, at the expense of power generated by a motor [11]. Such force develops from the interaction between the fluid and the geometry of the rotor. The geometry of the rotor is defined by diameter, number of blades, the propeller hub diameter and the hub angle β_{hub}. The propeller hub angle determines the advance per revolution swept by the propeller blades of any open rotor [11]. Fixed pitch propellers with fixed angles of advance per revolution have a set rotor performance that does not remain optimal for all flight segments of any vehicle [11]. Variable pitch propellers however vary the revolution swept during all flight conditions to any desired propeller pitch angle β_{pitch}, to cover a wide range of thrust magnitudes [11]. Another important parameter for propeller performance is the blade speed at the tip of the propeller given by the rotor blade tip Mach number M_{tip}. This magnitude is proportional to the diameter of the propeller as seen in the provided equation eq. 2.16.

$$M_{tip} = \sqrt{V_\infty^2 + \frac{wR_{prop}^2}{a_s}} \qquad (2.16)$$

Propeller design aims to reduce the tip Mach number in order to reduce the propeller noise on any operational RPM. The Aircraft performance module described in this methodology designs a rotor geometry if a rotor is not inputted into the model. The blade element momentum theory propeller design tool XROTOR was utilized for propeller design and segment thrust computation.

2.2.1 Propulsor Geometry Design and Performance

The propulsor performance is modeled for either a given input rotor geometry if available or a representative rotor designed uniquely for each vehicle architecture design condition.

Propulsor Geometry for AAM Vehicles

As described in Fig. 2.1, a design operating condition for the specified AAM mission requirements is used to design a rotor geometry in XROTOR. Such design condition is dependent on whether the AAM consists of a designed fixed or variable pitch rotor. For a variable pitch rotor, the operating point is selected from the performance takeoff and cruise conditions since the methodology for rotor design gives equal importance to achieving a good takeoff and climb angle, as well as, high cruise speeds. As suggested by Weick, a rotor with a design point about half-way in between the two extremes results in a rotor with good high-speed cruise performance while resulting in a takeoff roll nearly as short as the best takeoff rotor [11]. Thus for a variable pitch rotor, a midpoint magnitude of speed, thrust and RPM between the low and high-speed vehicle operative performance extremes is used for sizing. For

a fixed-pitch rotor, the operating design point however is selected as either from the takeoff or cruising performance conditions. For any vehicle, after a designed rotor geometry with a preliminary diameter, blade count, blade twist and chord per radial station, and the design point operating thrust, velocity and RPM is determined, the design point is shifted to match the unique performance characteristic of each AAM vehicle with a minimum rotor diameter to reduce M_{tip}, and thus reduce noise, within the design constraints.

Propulsor Performance

The flight segment rotor performance conditions, such as thrust, RPM, and pitch angle are obtained by modeling off-design conditions at the desired segment velocity and thrust condition (or desired RPM), for the rotor in the blade element momentum rotor theory design tool, XROTOR. The propeller thrust is plotted as a function of velocity and RPM to also obtain the feasible and unfeasible regions of operation based on the required thrust per segment.

Chapter 3

Propeller design, lift, drag and thrust sample demonstrations for AAM flight

3.1 Short takeoff and landing (STOL)

3.1.1 STOL Vehicle Characteristics

The Blown-Flap STOL vehicle used for analysis is assumed to operate similar to a conventional fixed wing aircraft and is presented in Fig. 3.1(a). In order to achieve short takeoff and landing field lengths, the Blown-Flap STOL vehicle utilizes distributed propulsion and blown flap technology, as described in [12]. The jet produced by the rotor wake, V_j, as noted in Fig. 3.2, increases the flow velocity at the flap, which provides higher C_L values.

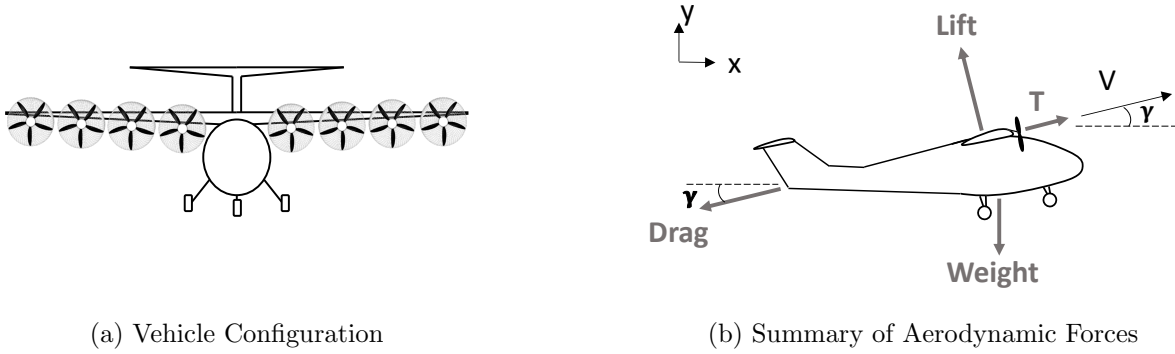(a) Vehicle Configuration   (b) Summary of Aerodynamic Forces

Figure 3.1: Vehicle Summary for Blown-Flap Short Takeoff and Landing (STOL)

As previously introduced in Chapter 2, blown lift also induces a unique source of drag from the blowing jet of the rotor wake. Such coefficient is added to the total drag buildup in this analysis. The thrust direction is otherwise assumed to follow the direction of flight, with flight path angle denoted as γ shown in Fig. 3.1.
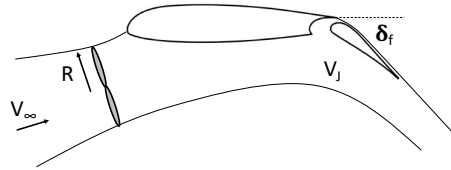

Figure 3.2: Rotor wake interaction with the flap in Blown-Flap STOL aircraft

A description of key vehicle properties used as inputs to model the flight performance, rotor blade geometry, and noise are described in Table 3.1, with aircraft characteristics, takeoff distance, and cruise speed used in the rotor design, and the known rotor geometries with the exception of the rotor diameter, taken found in [2]. Additional flap geometries and performance were taken from the sub-scale STOL demonstrator from [13], scaled to full-scale. The design takeoff thrust and cruise thrust per rotor were determined as described in Chapter 2, based on the design takeoff distance and speed, and design cruise speed, respectively. The vehicle was assumed to have a 150 ft takeoff field length, as indicated in [2]. A lift coefficient, C_L, of 6 was assumed during the departure, yielding a takeoff speed of 38 knots.

19

Table 3.1: Blown-Flap STOL vehicle properties, referenced from [2] and [13], used for performance analyses

Aircraft Characteristics	Weight (lbs)	6000
	Span (ft)	43.7
	Aspect Ratio	7.9
	Range (nmi)	348
	Number of Passengers	9
Known Rotor Geometry	Rotor Diameter (ft)	2.7**
	Number of Rotors	8
	Number of Blades per Rotor	5
	Hub Percent of Rotor Diameter (%)	25
Takeoff and Cruise Operating Points used for Rotor Design	Takeoff Distance (ft)	150
	Design Takeoff Thrust per Rotor (lb)*	229
	Design Takeoff Speed (knots)*	38
	Design Cruise Thrust per Rotor (lb)*	106
	Design Cruise Speed (knots)	152
Additional Considerations	Flap Settings	35° Takeoff
		65° Landing

*Determined from desired takeoff and cruise performance

**Diameter changed from [2] to lower tip Mach number

3.1.2 STOL Rotor Characteristics

To obtain the rotor geometry per blade section needed for any noise analysis, the rotors for this vehicle were designed with the methodology described in Chapter 2.2.1 for a variable pitch rotor. A preliminary design point was used between the thrust required for the 150

ft^2 takeoff ground roll and the design cruise thrust obtained at a speed of 152 knots. The Blown-Flap STOL rotor uniquely had to produce higher thrust magnitudes at lower speeds while having optimum efficiency during cruise. The midpoint design velocity was shifted to a lower speed to assure low-speed performance while simultaneously optimizing for cruise efficiency. In addition, rotor diameter was reduced to minimize M_{tip} to 0.392 and lower noise, as explained in Chapter 2.2.1. This results in a maximum RPM of 4000 for maximum takeoff thrust conditions with rotor design condition of a slow end of climb. A summary of the rotor properties is given in Table 3.2.

Table 3.2: Modeled Blown-Flap STOL rotor properties used for example performance analyses

Design Condition	Slow end of climb
Thrust per rotor at Design Condition (N)	1020
Velocity at Design Condition (m/s)	20
Power per rotor at Design Condition (kW)	48
RPM at Design Condition	3200
M_{tip} at Design Condition	0.392
Max RPM	4000
Rotor characteristics	Variable pitch
Rotor image	
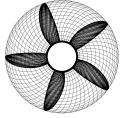
3.1.3 STOL Lift and Drag

The coefficient of lift is obtained by following the methodology from Chapter 2.1.1. The C_L for the cruise segment was assumed as 0.38, as suggested by [2]. The departure C_L of 6 was assumed from experimental data of high lift capabilities of STOL vehicles.

The total coefficient of drag discussed in Chapter 2.1.2 is plotted as a function of the throttle setting with a polynomial best-fit line in Fig. 3.3 and 3.4, and it includes the zero-lift drag, the induced drag and the drag due to blowing if applicable. The coefficient of drag due to blowing is added to the total drag coefficient only for the takeoff segment due to the low-speed deployment of leading-edge slats and trailing-edge flaps to achieve high lift as discussed in Chapter 2.1.2. The coefficient of induced drag C_{Di} was obtained to be 0.0059 for cruise.

(a) 100% Power

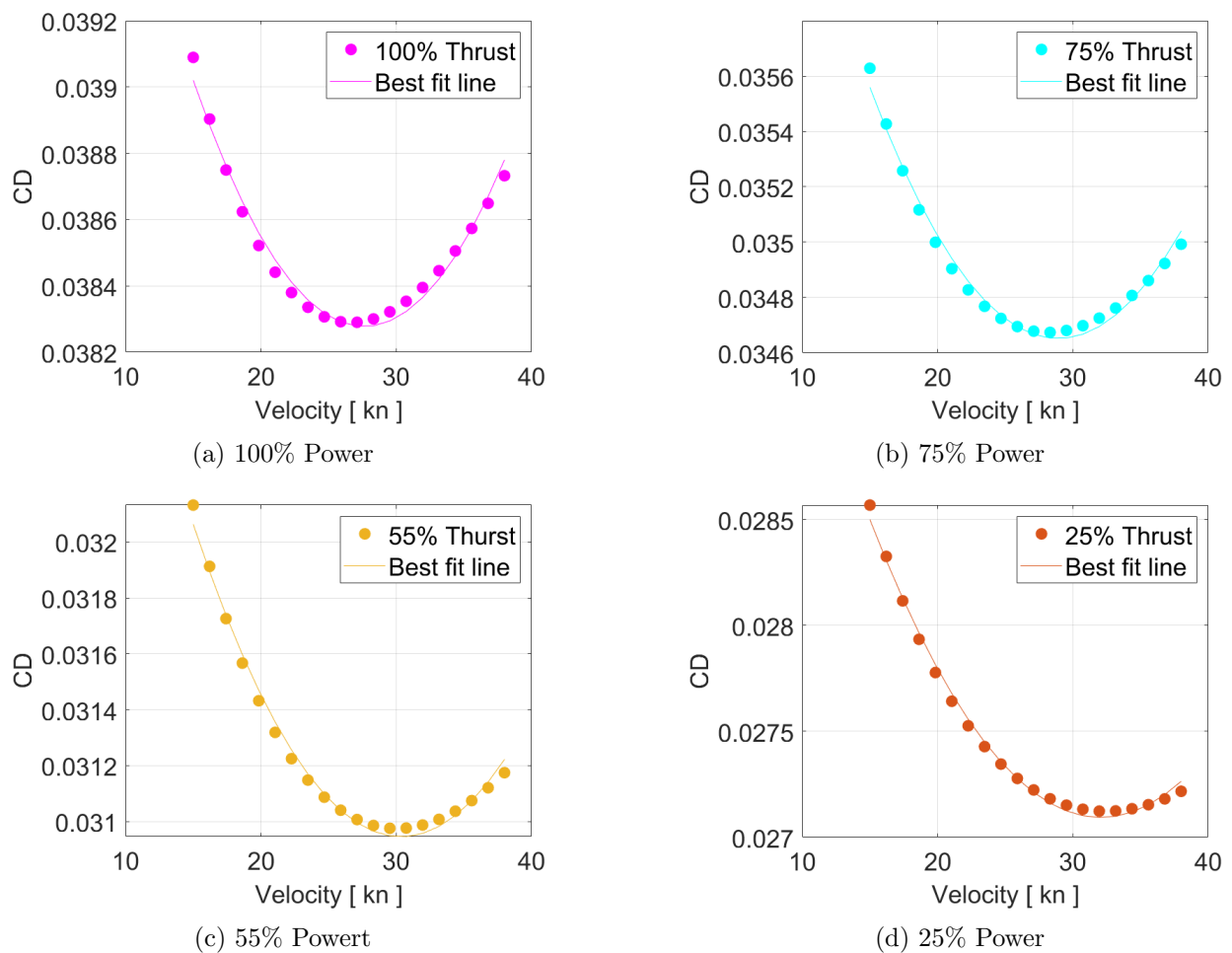(b) 75% Power

(c) 55% Powert

(d) 25% Power

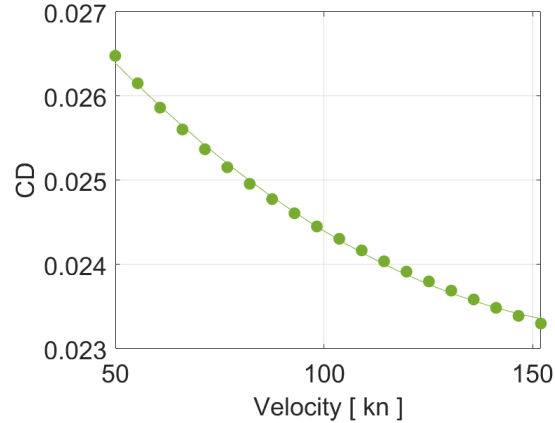Figure 3.3: Total drag coefficient for the STOL vehicle during the takeoff segment at power settings

Figure 3.4: STOL Coefficient of drag for short takeoff and landing (a) and cruise

The results shown in Fig. 3.3 and 3.4 show ranges in C_D from an overall takeoff maximum of 0.0392 to an overall minimum cruise of 0.023, depending on the flight speed and operation. As stated, the C_D values obtained in Fig. 3.3 contain the coefficient of drag due to blowing which was found to be the dominant drag form at 46.2% of the total drag coefficient at the maximum throttle takeoff speed. The maximum power takeoff shows a higher drag coefficient than the lower power settings of the rotors due to higher thrust and speed capabilities. The total drag coefficient for the low altitude cruise segment is found in Fig. 3.4 which shows a parabolic decreasing trend as velocity increases.

3.1.4   STOL Rotor Performance and Contour Maps

The propeller thrust is plotted as a function of velocity and RPM to obtain the STOL propeller feasible and unfeasible regions of operation, as described in Chapter 2.2.1. The fixed and variable pitch regions are swept to the maximum 4000 RPM, for STOL operation velocities ranging from 38 knots to 152 knots.

The STOL maximum power of 36,816 W was held constant as pitch varies, to obtain the range of thrust magnitudes for this propeller. The constant power propeller contour maps

for the STOL variable pitch propeller designed presented in Table 3.2 are shown in Fig. 3.5. As the percent power increases, more thrust is available at varying speeds for the same RPM ranges. A region of unfeasibility is seen in the lower left corner for the low-speed range, in the 25% thrust plot in Fig. 3.5(d).

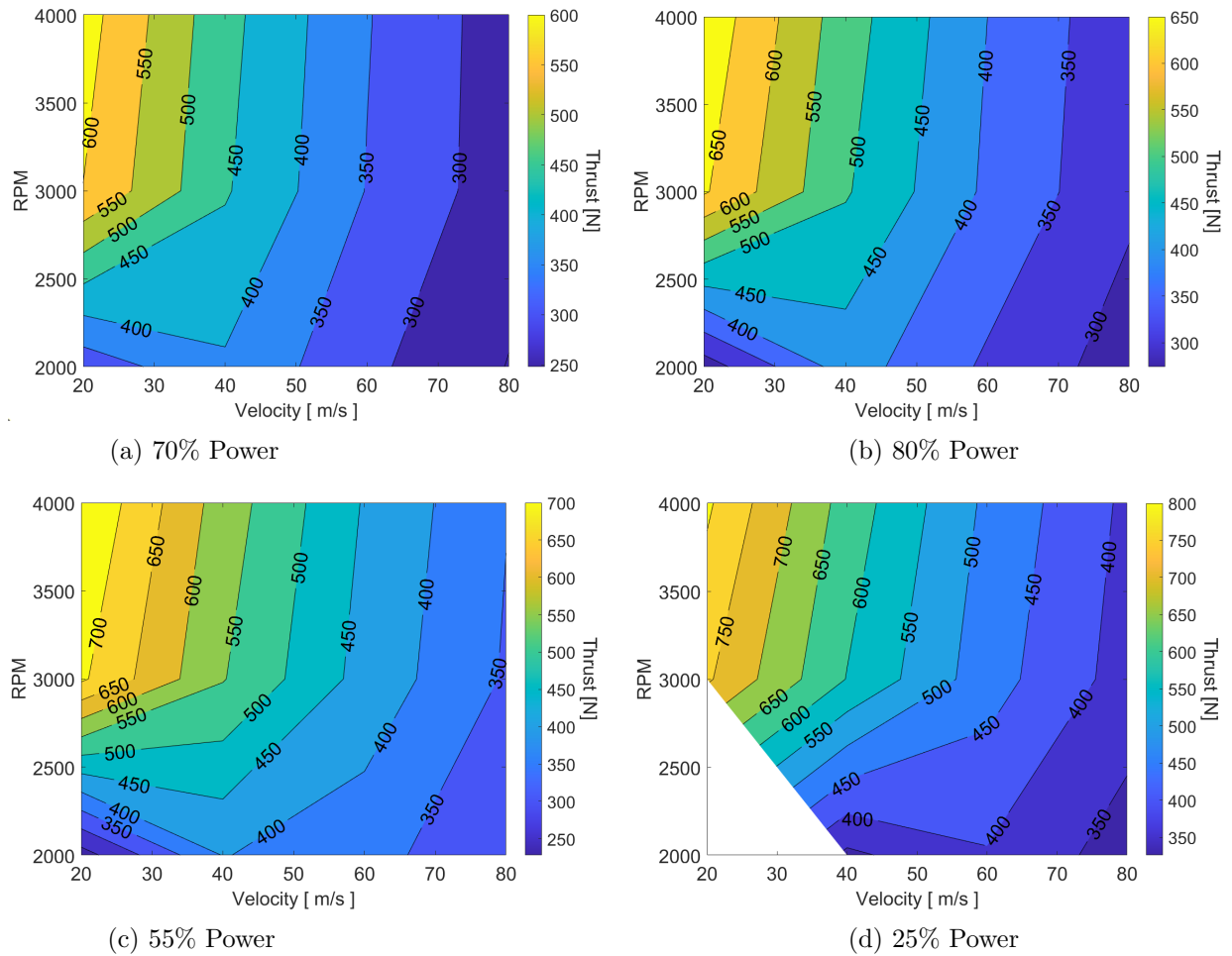(a) 70% Power

(b) 80% Power

(c) 55% Power

(d) 25% Power

Figure 3.5: STOL variable pitch 70%, 80%, 90% and 100% power plots

In addition, the hub pitch angle β_{pitch} is held constant from 60° to 90° to obtain the range of thrust magnitudes for this propeller. The constant β_{pitch} contour maps for the STOL variable pitch propeller presented in Table 3.2, are shown in Fig. 3.6. As the propeller pitch angle increases, more thrust is available at varying speeds for the same RPM ranges.
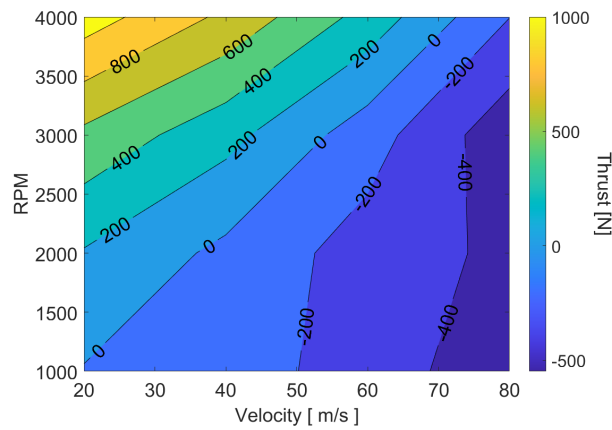
(a) 60° Hub
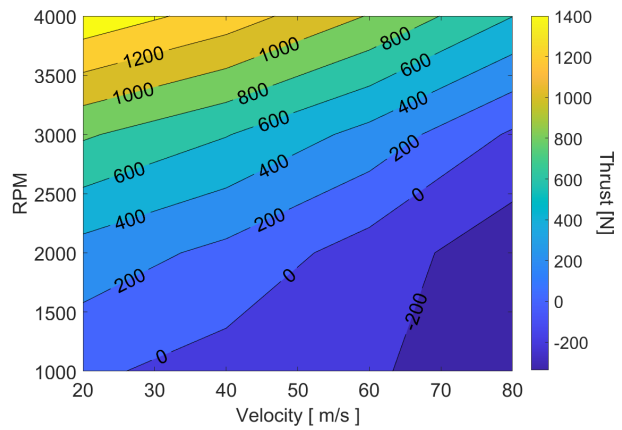
(b) 70° Hub
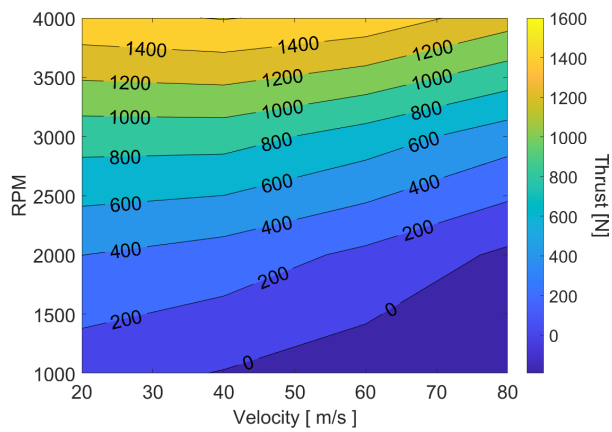
(c) 90° Hub

Figure 3.6: STOL fixed pitch 60°, 70°, 80° and 90° plots

3.2 Lift plus cruise (LPC) vertical takeoff and landing (VTOL)

3.2.1 LPC VTOL Vehicle Characteristics

The LPC-VTOL vehicle, diagramed in Fig. 3.7(a) is assumed to operate with two independent propulsive systems that govern the dynamics for vertical and forward flight, respectively. A horizontal thrust per rotor denoted T_x is achieved from horizontal propeller(s). Likewise, a vertical thrust per rotor, denoted T_y, is obtained from vertical rotor(s). The total thrust in the corresponding directions can be used to construct the flight profile according to eq. 2.1 and 2.2, as described in Chapter 2. The inertial properties of this vehicle are obtained by assuming this fixed directionality for each rotor disk throughout the flight procedure. The vehicle is assumed to remain level during all modes of flight, as seen in Fig. 3.7(b).

(a) Vehicle Configuration   (b) Summary of Aerodynamic Forces
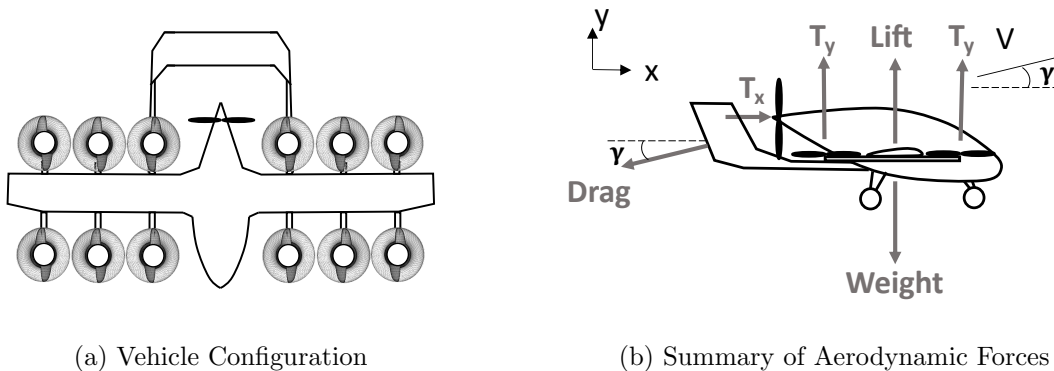
Figure 3.7: Vehicle Summary for LPC-VTOL

A description of key vehicle properties used to model the flight performance characteristics, rotor blade geometry, and noise are described in Table 3.3, with aircraft characteristics and rotor tip and hub diameter and blade count taken from [14]. The takeoff thrust and cruise thrust per lifting and cruising rotors used in the rotor design were determined as described in Chapter 2, based on the weight and design cruise speed, respectively. The vertical takeoff

26

thrust magnitude is assumed to be 1.3 times the vehicle weight while the design cruise thrust was obtained from the drag at the cruise speed of a 152 knots given in Table 3.3. These conditions were used to determine the takeoff and cruise rotor geometries, as discussed in Chapter 2.

Table 3.3: LPC-VTOL vehicle properties, referenced from [14], used for example performance analyses

|		
	Weight (lbs)	2800
	Span (ft)	36
Aircraft Characteristics	Aspect Ratio	12.4
	Range (nmi)	45.2
	Number of Passengers	2
	Rotor Diameter (ft)	Lift Rotors: 4.3
		Cruise Rotors: 6.6
	Number of Rotors	Lift Rotors: 12
		Cruise Rotors: 1
Known Rotor Geometry	Number of Blades per Rotor	Lift Rotors: 2
		Cruise Rotors: 1
	Hub Percent of Rotor Diameter (%)	Lift Rotors: 30
		Cruise Rotors: 20
	Takeoff Distance (ft)	0
	Design Takeoff Thrust per Rotor*	Lift Rotors: 303
		Cruise Rotors: 0
Takeoff and Cruise	Design Takeoff Speed (knots)**	38
Operating Points	Design Cruise Thrust per Rotor*	Lift Rotors: 0
used for Rotor Design		Cruise Rotors: 111
	Design Cruise Speed (knots)*	152

*Determined from desired takeoff and cruise performance

**Value assumed from Blown-Flap STOL vehicle example for rotor sizing

3.2.2 LPC VTOL Rotor Characteristics

To obtain the rotor geometry per blade section needed for any noise analysis, the lift rotors and cruise rotor were designed with the methodology described in Chapter 2.2.1 for fixed pitch rotors. The design takeoff and cruise thrust and velocity seen in Table 3.4 were selected to be the design conditions for the lift and cruise rotors, as previously stated. The rotor diameter was minimized for both the lift and cruise rotors to lower M_{tip} to 0.579 and 0.479 respectively. This results in an RPM of 2900 for the lift rotors and a cruise RPM of 1600 for the cruise rotor at the design conditions. A summary of the rotor properties is given in Table 3.4.

Table 3.4: LPC-VTOL rotor properties used for example noise analyses

| Rotor Type	Lifting Rotor	Cruising Rotor
Design Condition	Takeoff	Cruise
Thrust per rotor at Design Condition (N)	1350	500
Velocity at Design Condition (m/s)	20	50
Power per rotor at Design Condition (kW)	55.4	28.2
RPM at Design Condition	2900	1600
M_{tip} at Design Condition	0.579	0.479
Max RPM	2900	1600
Rotor characteristics	Fixed pitch	Fixed pitch
Rotor image		
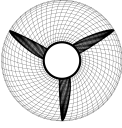
3.2.3   LPC VTOL Lift and Drag

The coefficient of lift is obtained by following the methodology from Chapter 2.1.1. The C_L for the cruise segment was assumed as 0.38 as suggested by [2]. The VTOL departure C_L was assumed to be negligible during the vertical takeoff segment. A NACA 0010 airfoil was assumed and a C_L of 0.4 was chosen for the transition segment, from an angle of attack of 4° above the zero lift angle of attack (α_0).

The zero-lift coefficient of drag discussed in Chapter 2.1 is plotted with a polynomial best-fit line for the VTOL segment seen in Fig. 3.8(a), the transition segment in 3.8(b) and for the cruise segment seen in 3.8(c). The coefficient of induced drag C_{Di} was obtained to be 0.0041 for transition and 0.0037 for cruise respectively. The coefficient of drag due to blowing does not apply to this AAM configuration due to the absence of a blowing wing distributed propulsion configuration.
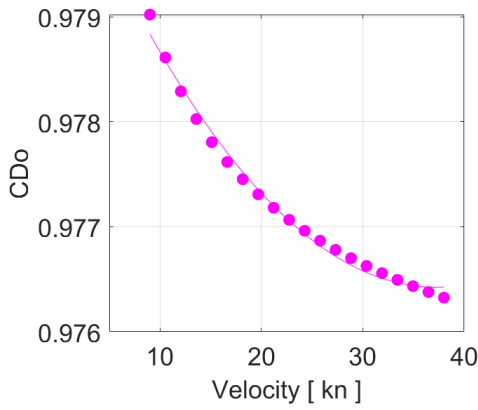
(a) VTOL segment with incoming velocity at the $\lambda_3=90°$
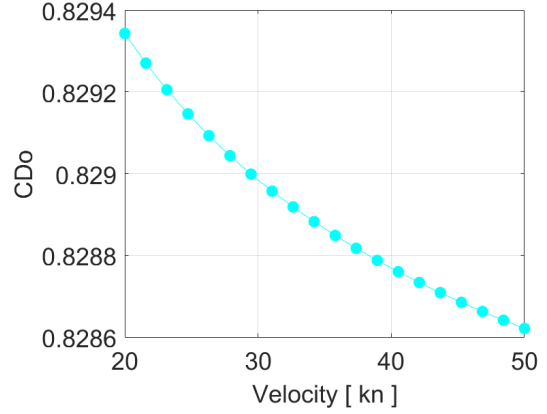
(b) Transition segment with incoming velocity at the $\lambda_3=45°$
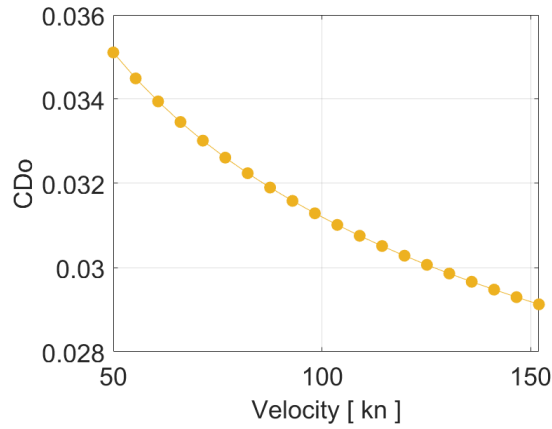
(c) Cruise segment with incoming velocity at the $\lambda_3=0°$

Figure 3.8: Zero lift drag coefficient C_{Do} for the LPC

The results shown in Fig. 3.8 show ranges in C_{Do} from an overall maximum of 0.979 during VTOL to a cruising overall minimum of 0.029, depending on the flight speed and operation. The total drag coefficient for the low-altitude cruise segment is found in Fig. 3.8(c). The overall vehicle parasitic (D_p) and induced drag force (D_i) are plotted for the VTOL and transition segments in Fig. 3.9(a), and the cruise segment in Fig. 3.9(b). The presented results show a decreasing parabolic trend as velocity increases, except for the induced drag during VTOL due to the absence of translational lift. The induced drag during transition is significantly lower in magnitude when compared to the other drag curves.
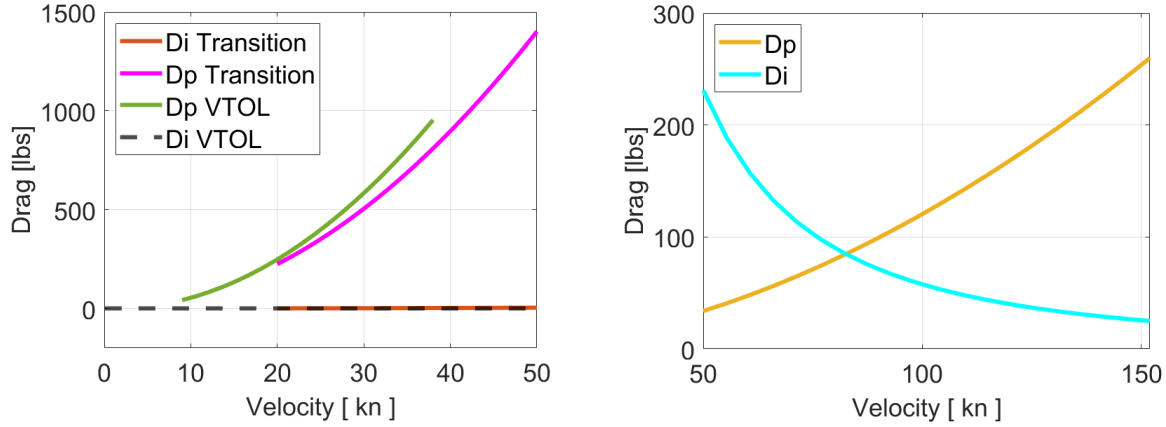
(a) VTOL and Transition with incoming velocity
at λ_3=90° and λ_2=45° respectively

(b) Cruise with incoming velocity at λ_1=0°

Figure 3.9: LPC VTOL parasitic drag (D_p) and induced drag (D_i) forces

3.2.4   LPC VTOL Rotor Performance and Contour Maps

The propeller thrust is plotted as a function of velocity and RPM to obtain the LPC VTOL propeller feasible and unfeasible regions of operation, as described in Chapter 2.2.1. The fixed pitch regions are swept to the maximum 2000 and 4000 RPM for the cruise and VTOL propellers, respectively. The contour map presented consists of the operation velocities ranging from 38 knots to 152 knots. The LPC maximum power was determined to be 98,272.2 W and 27,000 W for the cruise and VTOL rotors respectively, at fixed pitch hub angles. The fixed pitch thrust magnitudes are seen in Fig. 3.10(a) and (b), for the cruise and the VTOL propellers. The cruise propeller achieves a greater amount of thrust than the VTOL propeller at lower RPMs for velocities above the zero thrust line. Due to the lower speeds design point for the VTOL propellers, the VTOL propellers achieve less thrust for a greater range of RPMs. A region of unfeasibility is seen in the lower right corner of Fig. 3.10(a) for the higher speeds.
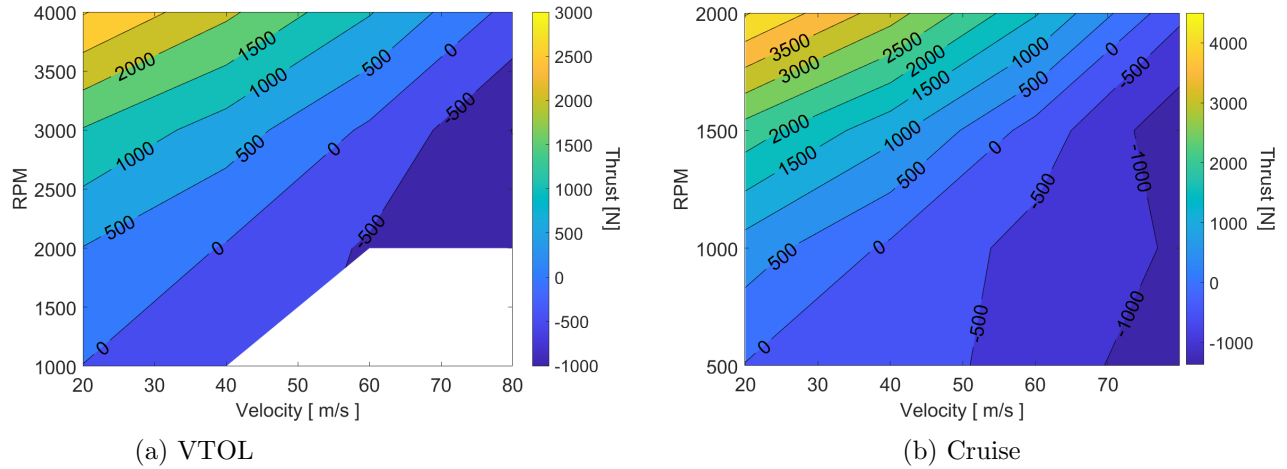
Figure 3.10: LPC VTOL fixed pitch plots

3.3 Tilt-Rotor vertical takeoff and landing (VTOL)

3.3.1 Tilt-Rotor VTOL Vehicle Characteristics

The Tilt-Rotor VTOL vehicle is assumed to operate with rotating rotors capable of providing thrust in the horizontal direction, vertical direction, or at an arbitrary angle of attack denoted by α, depending on the configuration setting. The x-direction and y-direction thrust per rotor, denoted by T_x and T_y, respectively are defined as the x and y components of the thrust vector per rotor, T, illustrated in Fig. 3.11. T_x and T_y can be used to construct the flight profile according to eq. 2.1 and eq. 2.2, as described in Chapter 2. The Tilt-Rotor VTOL vehicle is assumed to remain level during all modes of flight.

32
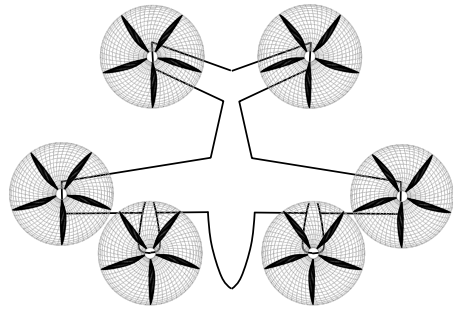
(a) Vehicle Configuration
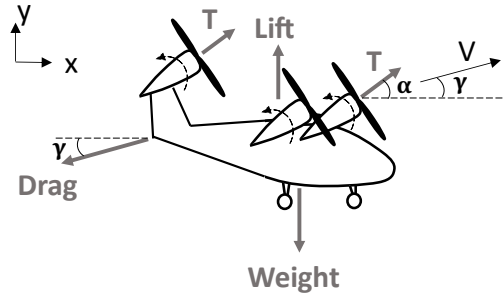
(b) Summary of Aerodynamic Forces

Figure 3.11: Vehicle Summary for Tilt-Rotor VTOL

A description of key vehicle properties used to model the flight performance characteristics, rotor blade geometry, and noise are described in Table 3.5, with aircraft characteristics and known rotor geometry used obtained from [15]. The takeoff and cruise operating points used in the rotor design, including the takeoff thrust and cruise thrust per lifting and cruising rotor, were determined as described in Chapter 2, based on the weight and design cruise speed, respectively. The vertical takeoff thrust magnitude is assumed to be 1.3 times the vehicle weight while the design cruise thrust speed was obtained from the drag at a 152 knots shown, as Table 3.3. These conditions were used to determine the rotor geometry as discussed in Chapter 2.2.1.

Table 3.5: Tilt-Rotor VTOL vehicle properties, referenced from [15], used for example performance analyses

	Weight (lbs)	4000
	Span (ft)	35
Aircraft Characteristics	Aspect Ratio	11.4
	Range (nmi)	130.3
	Number of Passengers	4
	Rotor Diameter (ft)	9.5
	Number of Rotors	6
Known Rotor Geometry	Number of Blades per Rotor	5
	Hub Percent of Rotor Diameter (%)	10
	Takeoff Distance (ft)	0
Takeoff and Cruise	Design Takeoff Thrust per Rotor (lb)*	350
Operating Points used	Design Takeoff Speed (knots)**	38
used for Rotor Design	Design Cruise Thrust per Rotor (lb)*	57
	Design Cruise Speed (knots)*	152

*Determined from desired takeoff and cruise performance

**Value assumed from Blown-Flap STOL vehicle example for rotor sizing

3.3.2   Tilt-Rotor VTOL Rotor Characteristics

To obtain the rotor geometry per blade section needed for the noise analysis, a rotor was designed with the methodology described in Chapter 2.2.1 for a variable pitch rotor. Following the same methodology as the Blown-Flap STOL rotor, a preliminary design point was obtained from the design takeoff and cruise conditions. In contrast with the STOL vehicle, the Tilt-Rotor VTOL rotor was uniquely required to perform a quiet hover and a powered

transition. The Tilt-Rotor VTOL midpoint thrust was shifted towards the low thrust condition to optimize the efficiency at higher speeds while lowering noise. The rotor diameter was minimized to lower operating rotor RPM and consequently lower noise M_{tip} to 0.379, as well as during the takeoff and cruise segments. This results in a maximum RPM of 800 with a design condition for transition flight. A summary of the rotor properties is given in Table 3.6.

Table 3.6: Tilt-Rotor VTOL rotor properties used for example performance analyses

Design Condition	Transition
Thrust per rotor at Design Condition (N)	1100
Velocity at Design Condition (m/s)	45
Power per rotor at Design Condition (kW)	55.4
RPM at Design Condition	800
M_{tip} at Design Condition	0.379
Max RPM	800
Rotor characteristics	Variable pitch
Rotor image	
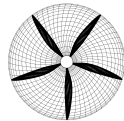
3.3.3 Tilt-Rotor VTOL Lift and Drag

The coefficient of lift is obtained by following the methodology from Chapter 2.1.1. The C_L for the cruise segment was assumed as 0.56, as suggested by [15]. The VTOL departure C_L was assumed to be negligible during the vertical takeoff segment. A NACA 0010 airfoil was assumed and a C_L of 0.4 was chosen for the transition segment, from an angle of attack of 4° above the zero lift angle of attack (α_0).

The zero-lift coefficient of drag discussed in Chapter 2.1.2 is plotted with a polynomial best-fit line for the VTOL, transition and cruise segment in Fig. 3.12. The coefficient of induced drag C_{Di} was obtained to be 0.0045 for transition and 0.0088 for cruise. The coefficient of drag due to blowing does not apply to this AAM configuration due to the absence of a blowing wing with distributed propulsion.
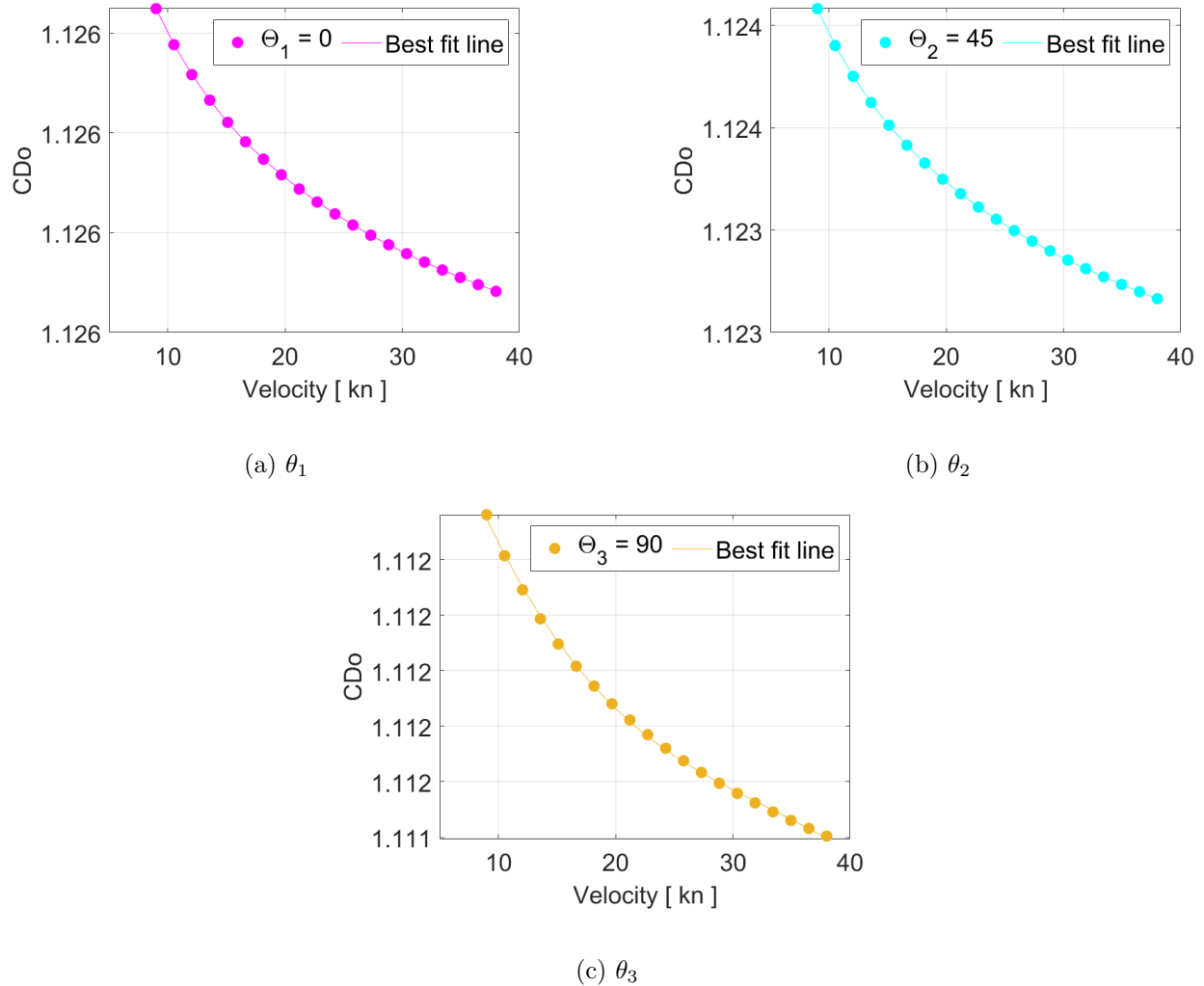

(a) θ_1

(b) θ_2

(c) θ_3

Figure 3.12: Zero lift drag coefficient C_{Do} for the Tilt-Rotor VTOL as the rotor tilt angle θ_i varies during the VTOL segment for an incoming velocity at the $\lambda_3=90°$

The results shown in Fig. 3.12 show a resulting high zero lift drag as pressure drag dominates the VTOL segment. A slightly higher C_{Do} is observed for the θ_1 tilt angle of the rotor. A low sensitivity variation was observed for the inclined aft pylons rotor tilt orientation due

to the dominance of drag obtained from the blunt wing, horizontal tail, and fuselage, in the incoming velocity normal direction.
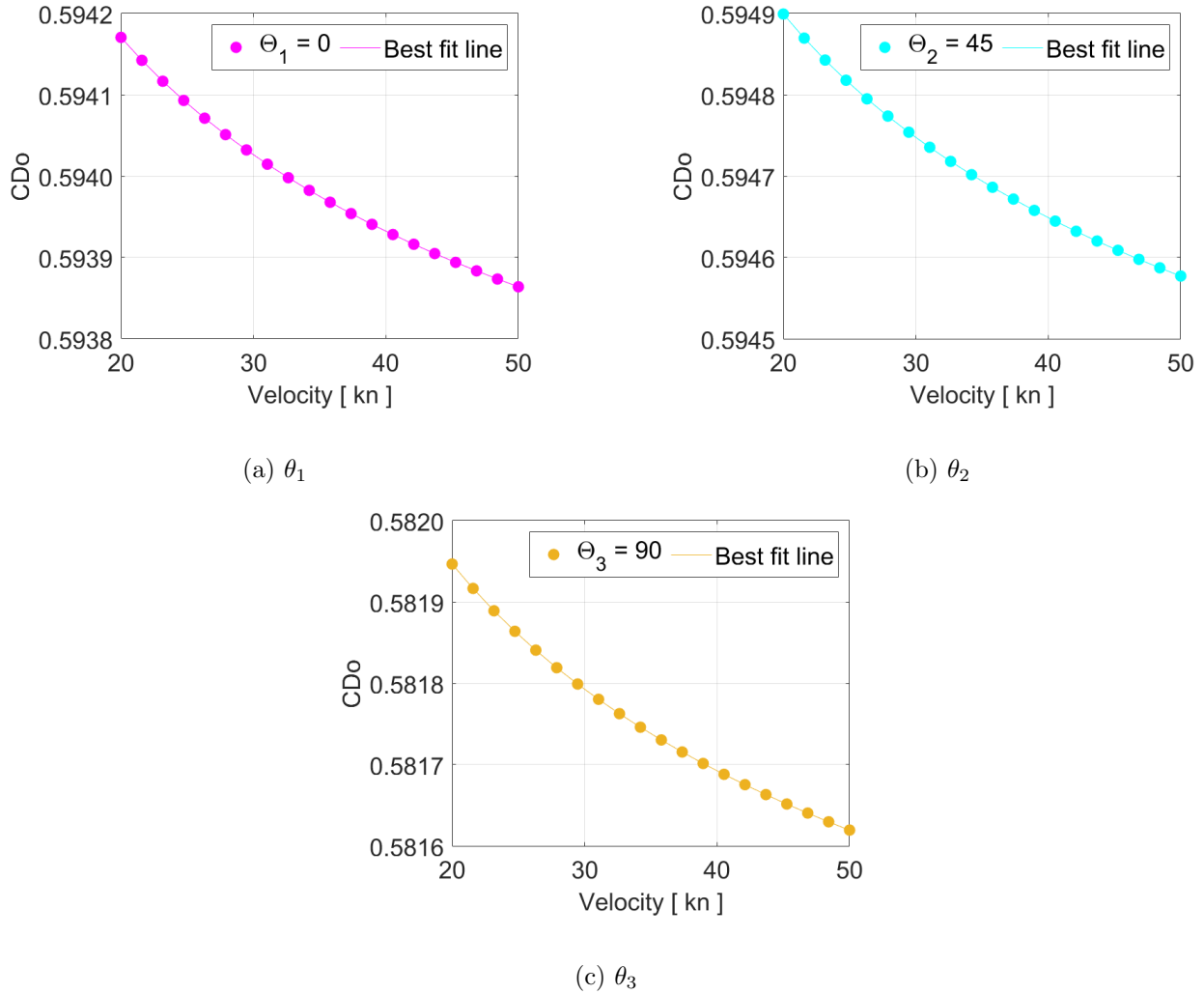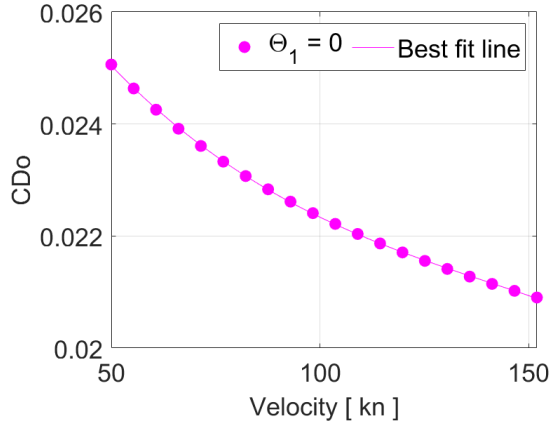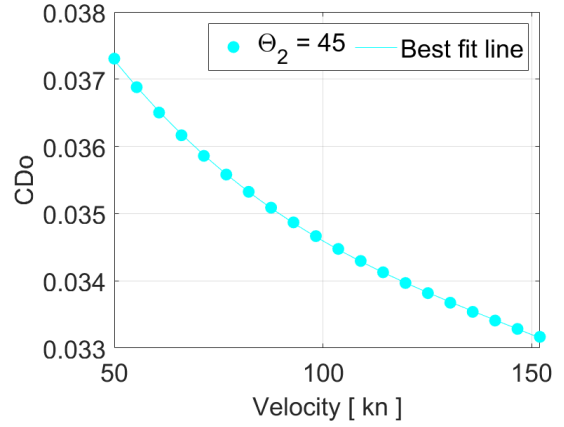

(a) θ_1
(b) θ_2

(c) θ_3

Figure 3.13: Zero lift drag coefficient C_{Do} for the Tilt-Rotor VTOL as the rotor tilt angle θ_i varies during the transition segment for an incoming velocity at the $\lambda_2=45°$
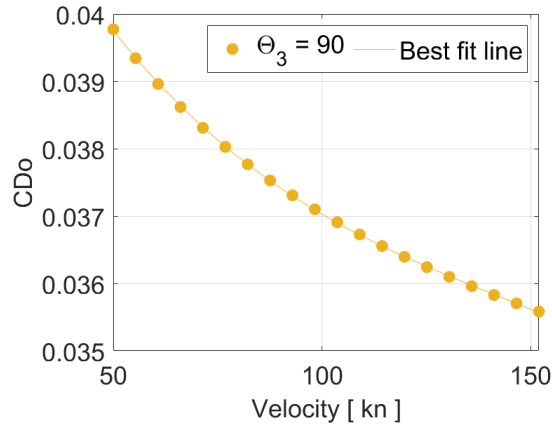
The results shown in Fig. 3.13 show a resulting partly high zero lift drag as both skin and pressure drag dominates in the high wind transition. A slightly higher C_{Do} is observed for the θ_2 tilt angle of the rotor. A low sensitivity variation was observed for the inclined pylon rotor tilt orientation due to the dominance of drag obtained from the wing, horizontal tail and fuselage, in the incoming velocity at a 45° flight path angle.

(a) θ_1

(b) θ_2

(c) θ_3

Figure 3.14: Zero lift drag coefficient C_{Do} for the Tilt-Rotor VTOL as the rotor tilt angle θ_i varies during the cruise segment for an incoming velocity at the $\lambda_1 = 0°$

The results shown in Fig. 3.14 show a resulting lower zero lift drag as skin friction drag dominates in the high speed cruise. A slightly higher C_{Do} is observed for the θ_3 tilt angle of the rotor. A slightly higher sensitivity variation was observed for the inclined pylon rotor tilt orientation due to the dominance of drag obtained from the blunt orientation change of the rotor when compared to the streamlined lifting surfaces and fuselage.

The overall vehicle parasitic (D_p) and induced drag force (D_i) are plotted for the VTOL and transition segments in Fig. 3.15(a), and the cruise segment in Fig. 3.15(b). All results

obtained show a decreasing parabolic trend as velocity increases, except the induced drag during VTOL due to the absence of translational lift. The induced drag during transition is significantly lower in magnitude when compared to the other drag curves.
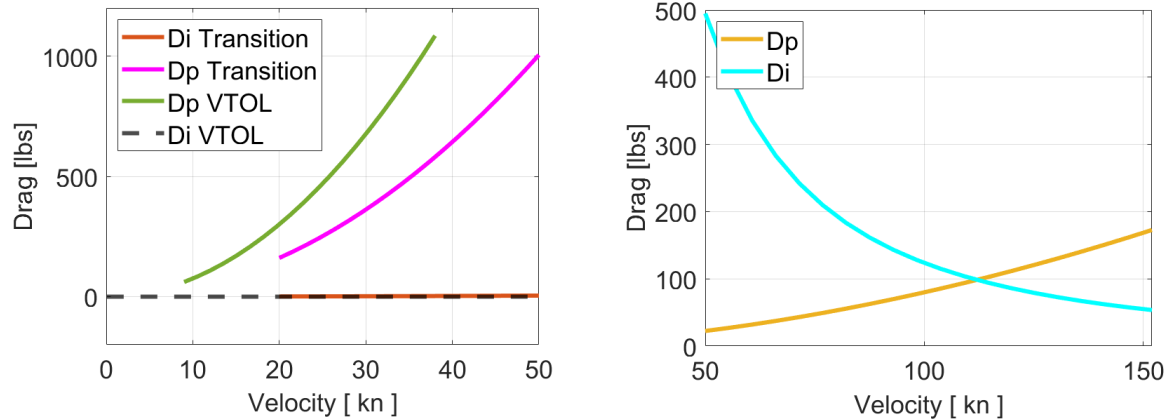

(a) VTOL at θ_3=90° and Transition at θ_2=45° with incoming velocity at λ_3=90°and λ_2=45° respectively
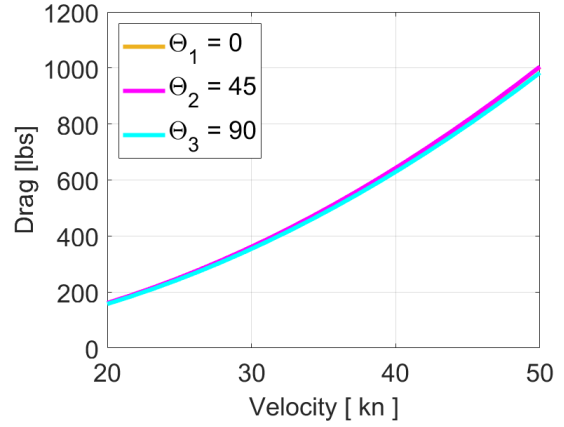
(b) Cruise at θ_1=0° with incoming velocity at λ_3=0°

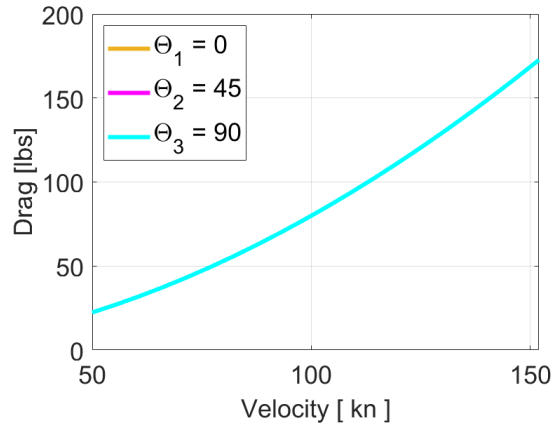Figure 3.15: Tilt-Rotor VTOL parasitic (D_p) and induced drag (D_i) forces

The drag force as a function of the rotor tilt angle variation is shown in Fig. 3.16. A low sensitivity is observed in the drag force when the propeller pylons are rotated for the variable pitch configurations. This result is consistent with the low variation in magnitude of the zero-lift drag coefficients found in Fig. 3.12, 3.13 and 3.14. The rotated inclined four aft pylons were found to be of 1% contribution to the total zero-lift drag coefficient obtained at the VTOL speed. A similar trend was found for the transition and cruise segments as seen in the plots below.
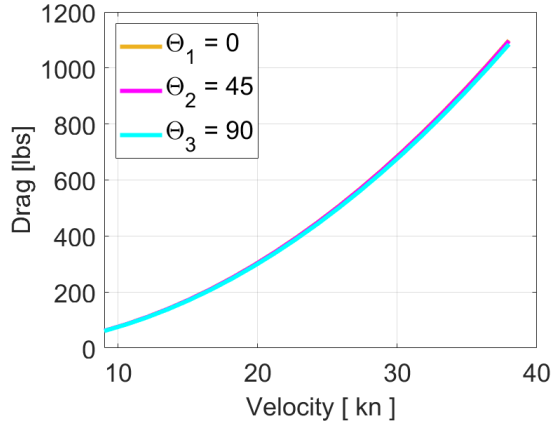
(a) VTOL with incoming velocity at $\lambda_1=90°$

(b) Transition with incoming velocity at $\lambda_2=45°$

(c) Cruise with incoming velocity at $\lambda_3=0°$

Figure 3.16: Tilt-Rotor VTOL parasitic (D_p) sensitivity to rotor tilt angle θ_i variation

3.3.4 Tilt-Rotor VTOL Rotor Performance and Contour Maps

The propeller thrust is plotted as a function of velocity and RPM to obtain the tilt-rotor propeller feasible and unfeasible regions of operation, as described in Chapter 2.2.1. The fixed and variable pitch regions are swept to the maximum 800 RPM, for the Tilt-Rotor VTOL operation velocities ranging from 38 to 152 knots.

The Tilt-Rotor VTOL maximum power of 77,102.8 W was held constant as pitch varies to

obtain the range of thrust magnitudes for this propeller. The constant power contour maps for the Tilt-Rotor variable pitch propeller designed presented in Table 3.6, are shown in Fig. 3.17. As the percent power increases, more thrust is available at varying speeds for the same RPM ranges.
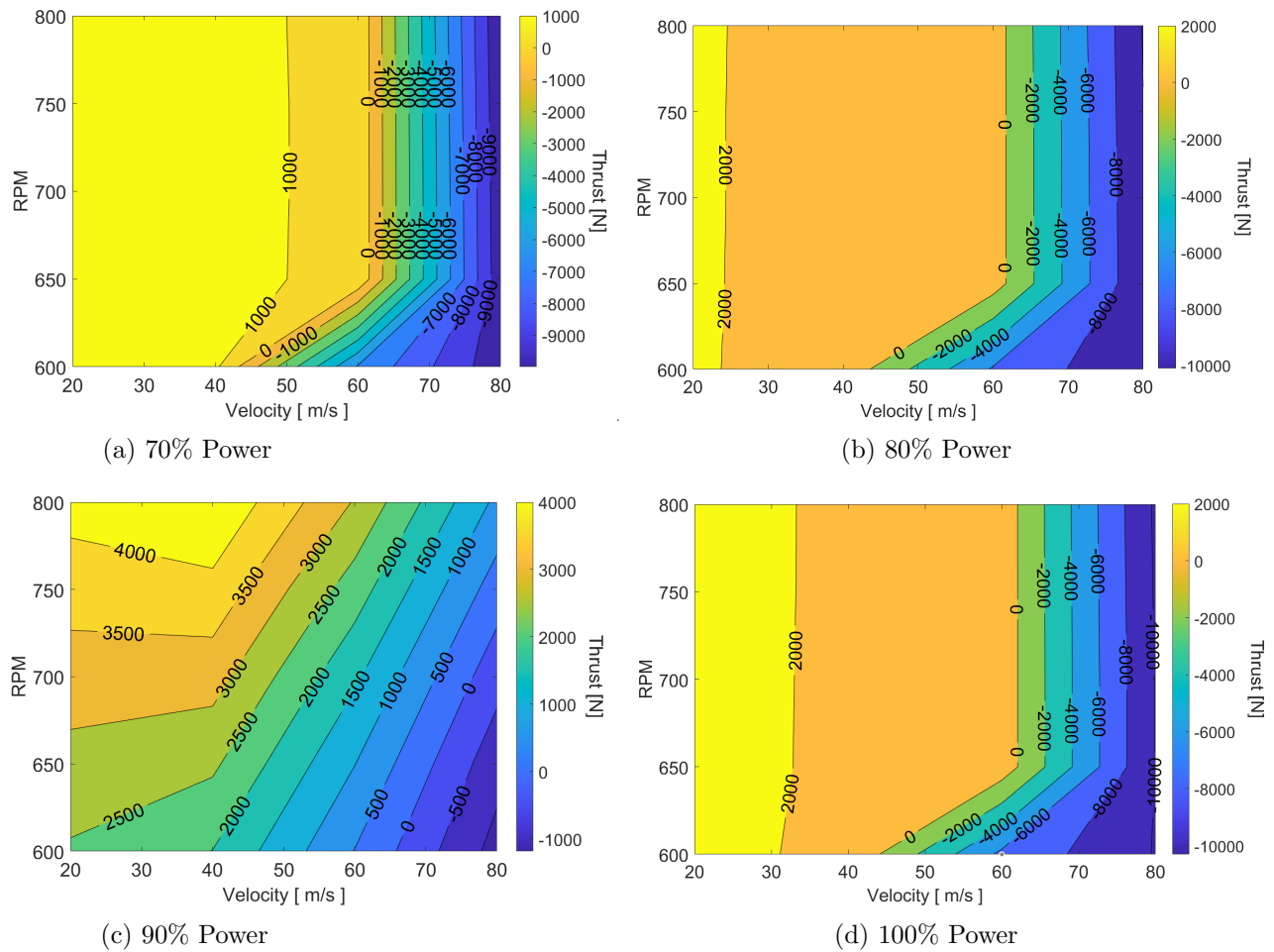

Figure 3.17: STOL variable pitch 70%, 80%, 90% and power plots

In addition, the hub pitch angle β_{pitch} is held constant from 60° to 90° to obtain the range of thrust magnitudes for this propeller. The constant hub pitch angle contour maps for the Tilt-Rotor VTOL variable pitch propeller are seen in Fig. 3.18. As the propeller pitch angle increases, more thrust is available at varying speeds for the same RPM ranges.
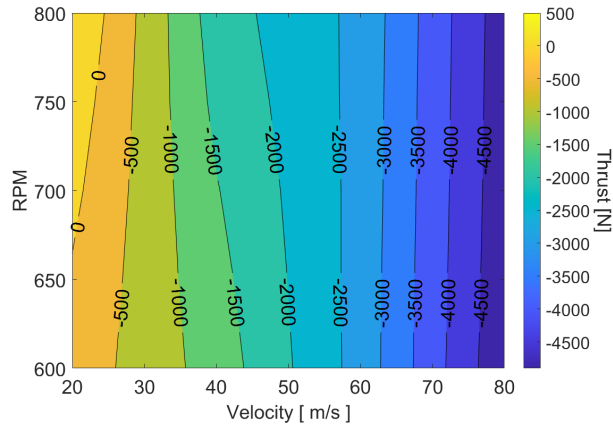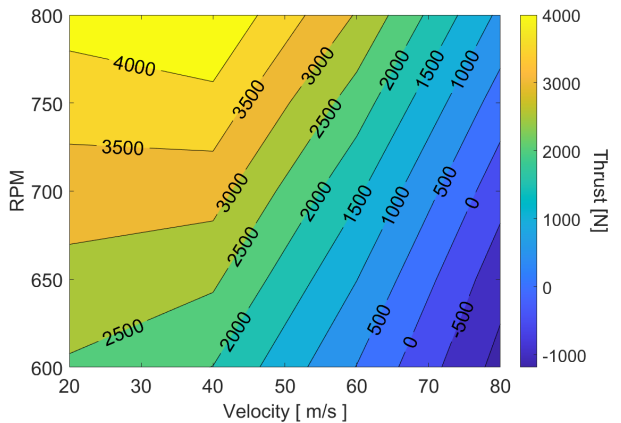
(a) 60° Hub
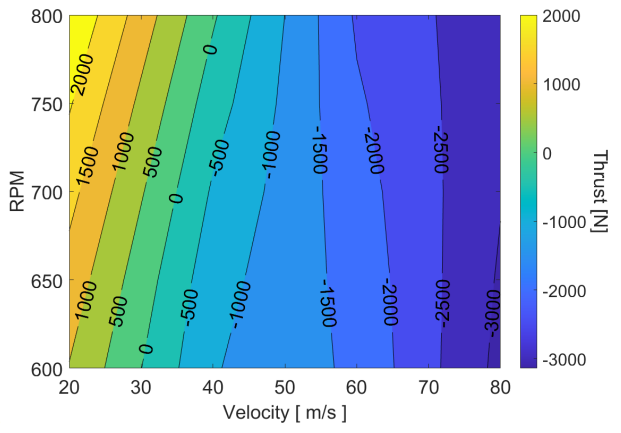
(b) 70° Hub
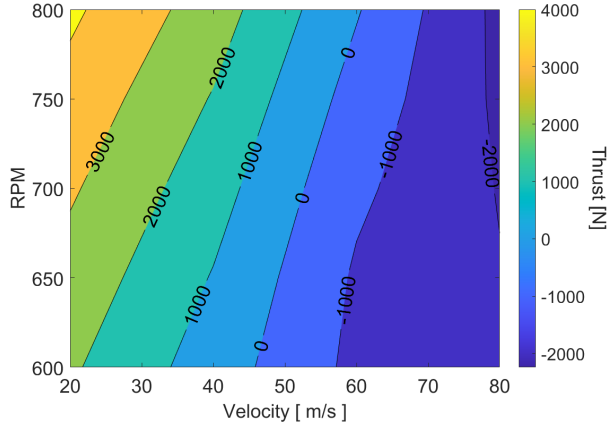
(c) 80° Hub

(d) 90° Hub

Figure 3.18: Tilt-Rotor VTOL fixed pitch 60°, 70°, 80° and 90° plots

Chapter 4

Conclusion

The methodology presented in this paper shows a preliminary capability to output aircraft performance of various types of AAM vehicles operating in VTOL, transition and cruise segments. Such methodology consists of a lift and drag model and a rotor performance and representative rotor geometry design model, that outputs rotor geometry for vehicle integration. These outputs such as velocity, RPM, and throttle setting, serve as inputs to any flight procedure and community noise modeling methods to predict AAM flight effects. The application of such methodology on the STOL, LPC VTOL and the Tilt-Rotor VTOL vehicles shows that various types of AAM geometries and architectures can be analyzed. Future work could also focus on VTOL experimental validation and data correlation either from subscale wind tunnel testing or industry partnerships. From these results, additional types of procedures, rotor designs, and vehicles could be analyzed and future flight procedures could be assessed and tailored to minimize community noise exposure.

Bibliography

[1] Rohit Goyal, Colleen Reiche, Chris Fernando, and Adam Cohen. Advanced air mobility: Demand analysis and market potential of the airport shuttle and air taxi markets. *Sustainability*, 13(13):7421, 2021.

[2] C. Courtin and *et al.* A performance comparison of estol and evtol aircraft. AIAA 2021-3220, AIAA Aviation 2021 Forum, 2021.

[3] N. Yeung and *et al.* Flight procedure and noise modeling of advanced air mobility flight vehicles. AIAA 2023, AIAA Aviation, 2023.

[4] L. V. Lopes and C. L. Burley. ANOPP2 user's manual: Version 1.2. NASA TM 2016-219342, 2016.

[5] R. S. Shevell. *Fundamentals of Flight.* Pearson, New Jersey, 1988.

[6] F. J. Rowe. *The Helio Courier Ultra C/STOL aircraft.* Jefferson, NC. McFarland & Company, Inc., 2006.

[7] N. Yeung and *et al.* Component noise modeling for distributed propulsion blown-flap stol vehicle flight procedures. AIAA 2022-3508, AIAA Aviation, 2022.

[8] C. Courtin. An assessment of electric stol aircraft, master's thesis. In *Massachusetts Institute of Technology*, 2019.

[9] S. F. Hoerner. *Fluid-Dynamic Drag.* Brick Town: Hoerner Fluid Dynamics, Great Britain, 1965.

[10] Gerhart A. L. Gerhart, P. M. and J Hochstein. *Munson, Young, and Okishi's Fundamentals of Fluid Mechanics.* Wiley,, 8th edition. edition, 2016.

[11] Fred E. Weick. *Aircraft Propeller Design.* McGraw-Hill Book Co, 1930.

[12] D. Agrawal and *et al.* Wind tunnel testing of a blown flap wing. AIAA 2019-3170, AIAA Aviation, 2019.

[13] C. Courtin, R. J. Hansman, and M. Drela. Flight test results of a subscale super-stol aircraft. AIAA 2020-0977, AIAA Scitech 2020 Forum, 2020.

[14] Alessandro Bacchini and Enrico Cestino. Electric VTOL Configurations Comparison. *Aerospace*, 6(3), 2019.

[15] Kyle A. Pascioni, Michael E. Watts, Mary Houston, Andrew Lind, James H. Stephenson, and Jeremy Bain. Acoustic Flight Test of the Joby Aviation Advanced Air Mobility Prototype Vehicle. In *28th AIAA/CEAS Aeroacoustics 2022 Conference*, Southampton, UK, 2022.